Extending the density functional embedding theory to finite temperature and an efficient iterative method for solving for embedding potentials

Chen Huang

Citation: The Journal of Chemical Physics **144**, 124106 (2016); doi: 10.1063/1.4944464
View online: http://dx.doi.org/10.1063/1.4944464
View Table of Contents: http://aip.scitation.org/toc/jcp/144/12
Published by the American Institute of Physics

Extending the density functional embedding theory to finite temperature and an efficient iterative method for solving for embedding potentials

Chen Huang[a)]
Department of Scientific Computing, Florida State University, Tallahassee, Florida 32306-4120, USA

(Received 22 November 2015; accepted 6 March 2016; published online 24 March 2016)

A key element in the density functional embedding theory (DFET) is the embedding potential. We discuss two major issues related to the embedding potential: (1) its non-uniqueness and (2) the numerical difficulty for solving for it, especially for the spin-polarized systems. To resolve the first issue, we extend DFET to finite temperature: all quantities, such as the subsystem densities and the total system's density, are calculated at a finite temperature. This is a physical extension since materials work at finite temperatures. We show that the embedding potential is strictly unique at $T > 0$. To resolve the second issue, we introduce an efficient iterative embedding potential solver. We discuss how to relax the magnetic moments in subsystems and how to equilibrate the chemical potentials across subsystems. The solver is robust and efficient for several non-trivial examples, in all of which good quality spin-polarized embedding potentials were obtained. We also demonstrate the solver on an extended periodic system: iron body-centered cubic (110) surface, which is related to the modeling of the heterogeneous catalysis involving iron, such as the Fischer-Tropsch and the Haber processes. This work would make it efficient and accurate to perform embedding simulations of some challenging material problems, such as the heterogeneous catalysis and the defects of complicated spin configurations in electronic materials. [http://dx.doi.org/10.1063/1.4944464]

I. INTRODUCTION

Local electronic structures and energetics are prerequisites for our understanding of important chemical processes in materials. Unfortunately, due to the many-body nature of the Schrödinger equation, it is computationally infeasible to apply accurate quantum mechanics methods to large scale materials. Multi-scale quantum mechanics methods are therefore invaluable for helping us gain insight into the local electronic structures in materials. When performing multi-scale modelings, one often partitions a system into two subsystems: the region of interest (called cluster in this work) and its environment. One conceptual difficulty is how to partition the many-body wave-function, since in principle a wave-function cannot be partitioned. Fortunately, in practice, electronic structure at one location is not affected much by a perturbing potential far away, i.e., the "nearsightedness" principle of the quantum mechanics.[1,2] This nearsightedness principle is believed to be one of several reasons for the great success of the local density approximation (LDA) and the generalized gradient approximation (GGA) widely used in the density functional theory (DFT)[3,4] calculations. Nearsightedness principle is also the foundation of many linear-scaling Kohn-Sham (KS) DFT methods.[5,6]

Many schemes exist for performing multi-scale quantum mechanics simulations. For ionic systems, such as oxides, the partitioning is straightforward. Point charges or shell-models[7,8] can be used to represent the electrostatic potential due to background ions. For covalent materials, the capping atoms[9] and the pseudo-bond[10] method have been used to saturate the dangling bonds due to cutting covalent bonds. By matching the wave functions at the interface between adjacent subsystems, an environment can be replaced by an energy-dependent embedding potential.[11,12] Inspired by the pseudopotential techniques, a cluster can be solved by enforcing its orbitals to be orthogonal to the orbitals of its environment.[13] In the density matrix embedding theory, the electronic structure of a cluster is solved by performing correlated wave-function (CW) methods in the active space constructed by projecting the total system's molecular orbitals into the cluster's Hilbert space.[14] Different from the traditional complete active space self-consistent field method, in the density matrix embedding theory, a potential is applied to the bath to better mimic the true bath.

In the past two decades, the density functional embedding theory (DFET)[15–19] has become a powerful method for calculating the local energetics and electronic structures in materials. DFET has been successfully applied to many challenging surface problems, including explaining the adsorption of carbon monoxide on copper surface,[20] resolving the controversial mechanism of aluminum oxidation,[21] and shedding light on the plasmon-assisted hydrogen dissociation on gold nanoparticles.[22] The basic idea of DFET is that we partition a system's electron density into subsystem densities. After the partitioning, a cluster is defined and is solved by a high-level method, with its environment replaced by a local embedding potential. The development of DFET was inspired by the early pioneering works on the subsystem DFT[23–25] and the frozen density embedding (FDE).[26,27] Details about the subsystems DFT, FDE, and DFET have been reviewed.[18,28–32]

a)chuang3@fsu.edu

Embedding potentials were evaluated by approximating the kinetic part of the interaction between a cluster and its environment with certain kinetic energy density functionals.[15,16,26,33–38] First-principle embedding potentials were obtained by inverting the KS equation.[39–42] The non-uniqueness of embedding potentials (called the reactivity potential in Ref. 43) was discussed and removed by Cohen and Wasserman in their study of the chemical reactivity.[43] A similar approach was taken to tackle the non-uniqueness of embedding potentials in the context of DFET, and an optimized effective potential (OEP) method was developed for calculating embedding potentials.[20]

In this work, we address two major issues related to the embedding potential: (1) its non-uniqueness and (2) the numerical challenges in calculating it, especially for the spin-polarized materials. The non-uniqueness of an embedding potential was previously removed under certain assumptions. In Ref. 20, the assumption was that subsystems need to be non-degenerate. In Ref. 43, the assumption was that the sum of subsystem energy functionals needs to be non-degenerate. These assumptions can easily break down in practice, since degenerate quantum systems are common in practice. On the other hand, the degeneracy of a quantum system does not cause much trouble in DFT, since the total energy stays the same for different degenerate states, and we simply solve for a state out of several degenerate ground states.[44] In embedding simulations, a non-unique embedding potential can yield different results. For example, different embedding potentials might yield different adsorption energies for molecules adsorbed on metals. The non-uniqueness of embedding potential therefore makes embedding simulations non-tractable. The second issue is that to calculate the embedding potentials we need to perform self-consistent KS-DFT calculations on subsystems during solving the OEP problem.[20] If the convergence of these KS-DFT calculations is difficult to reach, the OEP problem is numerically difficult to solve.

In this work, I remove the non-uniqueness of embedding potentials by extending DFET to the finite temperature. This extension does not narrow down the scope of its applications, since materials work at finite temperature. To resolve the second issue above, we develop an iterative method that does not require performing self-consistent KS-DFT calculations on subsystems. The robustness and efficiency of this new iterative method is demonstrated on several high-spin systems.

II. EXTENDING THE DENSITY FUNCTIONAL EMBEDDING THEORY TO FINITE TEMPERATURE

A. The density functional embedding theory

We briefly summarize several key points of DFET. It tackles difficult electronic structure problems in a divide-and-conquer manner.[18,19] We divide the total system into several subsystems (the step 1 in Fig. 1). We take the carbon monoxide (CO) adsorbed on copper surface as an example. We group atoms into two subsystems. The cluster (subsystem 1) contains the CO molecule and several Cu atoms underneath. The rest of the Cu atoms are considered as the environment (subsystem 2). In the step 2, the total electron density $n_{total}(\vec{r})$ is decomposed to the cluster's density $n_{cluster}(\vec{r})$ and the environment's density $n_{env}(\vec{r})$. The total energy is then formally decomposed as

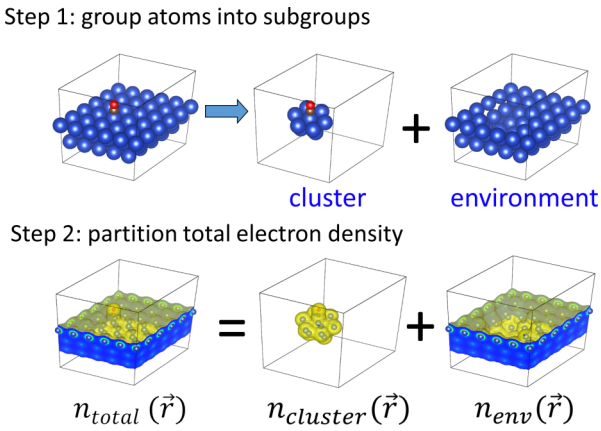

FIG. 1. An illustration of the density functional embedding theory. The red atom is oxygen. The brown atom is carbon. The blue atoms are copper. $n_{cluster}(\vec{r})$, $n_{env}(\vec{r})$, and $n_{total}(\vec{r})$ are the electron densities of the cluster, the environment, and the total system, respectively. The partitioning satisfies the constraint $n_{total} = n_{cluster} + n_{env}$.

$$E_{total} = E_{cluster}[n_{cluster}] + E_{env}[n_{env}] + E_{int}[n_{cluster}, n_{env}], \quad (1)$$

where E_{int} is the interaction energy between cluster and environment. Based on the energy decomposition, the embedding potential that the environment exerts on the cluster is formally defined as $V_{emb}^{cluster}(\vec{r}) = \delta E_{int}/\delta n_{cluster}(\vec{r})$, and the embedding potential that the cluster exerts on its environment is $V_{emb}^{env}(\vec{r}) = \delta E_{int}/\delta n_{env}(\vec{r})$.

Since it is the total electron density that determines the entire system, the sum of the subsystem electron densities should be equal to the total electron density, i.e., $n_{total} = n_{cluster} + n_{env}$. Apparently, any partitioning of the total electron density is, in principle, valid, as long as the sum of subsystem electron densities matches the total electron density n_{total}. This non-uniqueness has been removed[20,43] by employing an additional constraint $V_{emb}^{cluster}(\vec{r}) = V_{emb}^{env}(\vec{r}) \equiv V_{emb}(\vec{r})$: all subsystems share the same embedding potential. The major task is then to solve for this common embedding potential $V_{emb}(\vec{r})$.

B. Extending the density functional embedding theory to finite temperature

To extend DFET to the finite temperature, the total electron density n_{total} and the subsystem electron densities are all calculated at a finite temperature. Since subsystem can no longer be degenerate at $T > 0$,[45,46] the assumption in our previous proof[20] that subsystems must be non-degenerate can be removed. There are several ways to extend the descriptions of subsystems to a finite temperature. A subsystem can be treated by (a) the grand canonical ensemble, (b) the grand canonical ensemble with a fixed electron number, and (c) the canonical ensemble. In the following, we show that embedding potential is strictly unique in all cases.

1. Subsystems are treated using the grand canonical ensemble and have a common chemical potential

We consider the case that a system is decomposed into two subsystems: A and B. Our discussion can be generalized to multiple subsystems. To prove the uniqueness of the embedding potential, let us assume that there are two embedding potentials V_{emb} and V'_{emb}, both of which give the $n_{total}(\vec{r})$. V_{emb} gives the subsystem density matrices, $\{\rho_A, \rho_B\}$ and V'_{emb} gives the subsystem density matrices, $\{\rho'_A, \rho'_B\}$. The global chemical potentials are μ and μ', respectively.

Following Mermin[45] and our previous work,[20] for the subsystem A, we have

$$\begin{aligned}\Omega'_A &= \mathrm{Tr}\rho'_A\left(H'_A - \mu' N + \frac{1}{\beta}\ln\rho'_A\right)\\ &< \mathrm{Tr}\rho_A\left(H'_A - \mu' N + \frac{1}{\beta}\ln\rho_A\right)\\ &= \Omega_A + \mathrm{Tr}\rho_A(V'_{emb} - V_{emb}) + Q_A(\mu - \mu'),\end{aligned} \tag{2}$$

where N is the electron number operator and H'_A is the Hamiltonian of the subsystem A plus V'_{emb}. Q_A is the electron number of the subsystem A. Similarly, we have for the subsystem B,

$$\Omega'_B < \Omega_B + \mathrm{Tr}\rho_B(V'_{emb} - V_{emb}) + Q_B(\mu - \mu'). \tag{3}$$

Summing up above two equations, we have

$$\begin{aligned}\Omega'_A + \Omega'_B < \Omega_A + \Omega_B + \int d\vec{r} n(\vec{r})(V'_{emb}(\vec{r}) - V_{emb}(\vec{r}))\\ + Q_{total}(\mu - \mu').\end{aligned} \tag{4}$$

By interchanging the primed and unprimed cases, we have

$$\begin{aligned}\Omega_A + \Omega_B < \Omega'_A + \Omega'_B + \int d\vec{r} n(\vec{r})(V_{emb}(\vec{r}) - V'_{emb}(\vec{r}))\\ + Q_{total}(\mu' - \mu).\end{aligned} \tag{5}$$

Summing Eqs. (4) and (5), we have $0 < 0$, which is false. Thus, if subsystems are treated using the grand canonical ensemble and have the same chemical potential, there is only one embedding potential (one density partitioning) for a given total electron density. Our proof does not require the assumption that subsystems are non-degenerate,[20] or the sum of subsystems is non-degenerate.[43]

2. Subsystems are treated using the grand canonical ensemble and the electron numbers in subsystems are fixed

Subsystems can be solved using KS-DFT employing advanced orbital-dependent exchange-correlation (XC) functionals, such as the exact-exchange (EXX) and the correlation based on the random phase approximation (RPA).[47] In practice, we would like to fix subsystems' electron numbers to integers, since fractional electron number can cause the self-interaction error,[48,49] even with some advanced XC functionals, such as the EXX+RPA.[50]

We consider the case that subsystems are treated using the grand canonical ensemble, and their electron numbers are fixed. Following a similar procedure, we show in Appendix A that the resulted embedding potential is also strictly unique.

3. Subsystems are treated using the canonical ensemble

Another way to extend subsystems to finite temperature is to treat them using the canonical ensemble. The Helmholtz free energy is[51]

$$A[\rho] = \mathrm{Tr}\rho(H + \frac{1}{\beta}\ln\rho), \tag{6}$$

where ρ is the density matrix. The stationary point of $A[\rho]$ is

$$\rho_0 = \exp(-\beta H)/\mathrm{Tr}\exp(-\beta H),$$

which is the unique minimum of $A[\rho]$ (proved in Appendix B): $A[\rho] > A[\rho_0]$ for any $\rho \neq \rho_0$. We now show that the resulted embedding potential is also unique.

Again let us assume that there are two embedding potentials V_{emb} and V'_{emb}, such that they produce the same total electron density. Similar to the previous proof, we have

$$\begin{aligned}A'_A &= \mathrm{Tr}\rho'_A(H'_A + \frac{1}{\beta}\ln\rho'_A)\\ &< \mathrm{Tr}\rho_A(H'_A + \frac{1}{\beta}\ln\rho_A)\\ &= A_A + \int dr^3(V'_{emb}(\vec{r}) - V_{emb}(\vec{r}))n_A(\vec{r}).\end{aligned} \tag{7}$$

For the subsystem B, we have

$$A'_B < A_B + \int dr^3(V'_{emb}(\vec{r}) - V_{emb}(\vec{r}))n_B(\vec{r}). \tag{8}$$

Summing up the two inequalities, we have

$$\begin{aligned}A'_A + A'_B < A_A + A_B\\ + \int dr^3(V'_{emb}(\vec{r}) - V_{emb}(\vec{r}))n_{total}(\vec{r}).\end{aligned} \tag{9}$$

By interchanging the primed and unprimed cases, we have

$$\begin{aligned}A_A + A_B < A'_A + A'_B\\ + \int dr^3(V_{emb}(\vec{r}) - V'_{emb}(\vec{r}))n_{total}(\vec{r}).\end{aligned} \tag{10}$$

Summing Eqs. (9) and (10), we obtain $0 < 0$, which is false. Therefore there is only one embedding potential (if it exists) that partitions the total electron density into two subsystem electron densities.

III. METHODS FOR SOLVING FOR EMBEDDING POTENTIALS

After removing the non-uniqueness of embedding potentials by extending DFET to finite temperature, we discuss how to efficiently solve for embedding potentials, which is a key input for embedded cluster calculations.

A. Optimized effective potential method for solving for embedding potentials

We recently proposed an OEP method for calculating embedding potentials.[20] In that OEP method, we define a W functional in terms of $V_{emb}(\vec{r})$,

$$W = \sum_K E_K[V_{emb,\sigma}] - \sum_{\sigma=\alpha,\beta} \int dr^3 n^{ref}_{total,\sigma}(\vec{r}) V_{emb,\sigma}(\vec{r}). \quad (11)$$

$n^{ref}_{total,\sigma}(\vec{r})$ is the reference electron density obtained by performing calculations on the total system in advance. For example, $n^{ref}_{total,\sigma}(\vec{r})$ can be obtained by performing KS-DFT-LDA on the total system. E_K is the energy of the subsystem K, with the Hamiltonian $\hat{H}'_K = \hat{H}_K + \hat{V}_{emb}$, where $\hat{H}_K$ is the original Hamiltonian of the subsystem K. E_K is then a functional of V_{emb}. Any method can be employed to solve $\hat{H}'_K$ (such as KS-DFT-LDA), as long as the method outputs electron density and energy which are needed to calculate the W and its gradient[20]

$$g_\sigma(\vec{r}) \equiv \frac{\delta W}{\delta V_{emb,\sigma}(\vec{r})} = \sum_K n_{K,\sigma}(\vec{r}) - n^{ref}_{total,\sigma}(\vec{r}). \quad (12)$$

In Ref. 20, we showed that we have $\sum_K n_K = n^{ref}_{total}$, once the W is maximized.

Here, we consider a special case that all subsystems are solved by KS-DFT and $n^{ref}_{total,\sigma}$ is also obtained using KS-DFT. The accuracy of $V_{emb,\sigma}$ is then determined by the XC functional used in these KS-DFT calculations. Since KS-DFT is often solved in an iterative way,[52] subsystem KS-DFT can have difficulty to converge in practice. If subsystem's KS-DFT does not converge, the gradient for maximizing the W functional will have error, making it difficult to maximize the W. We have observed such numerical difficulty in practice.

B. An iterative method for solving for embedding potentials

Inspired by the popular iterative scheme for solving KS-DFT,[52] we introduce an iterative method for calculating embedding potentials. The basic idea is to first maximize the W functional with the subsystem KS potentials *fixed*. After that, we update subsystems' KS potentials. At self-consistency, we obtain the same results as solving the original OEP problem (Eq. (11)).

A flowchart for our iterative method is shown in Fig. 2. In the step 1, the reference electron density is given. In the step 2, the subsystem KS potentials are constructed from the trial subsystem Hartree + XC potentials $\{V_{hxc,K}\}$. In the step 3, the W functional is maximized for the fixed $\{V_{hxc,K}\}$. In the step 4, V_{emb} and new subsystem electron densities are obtained from the step 3. In the step 5, $\{V_{hxc,K}\}$ are updated. $V_{xc,K}$ can be easily calculated based on the subsystem densities $n_K(\vec{r})$, if density-based XC functionals, such as LDA and GGA, are used. For those orbital-based XC functionals, $V_{xc,K}$ can be obtained by solving the OEP equation.[53] In the step 6, we check the convergence of $V_{hxc,K}$. To accelerate the convergence, some mixing schemes, such as the Anderson mixing[54] or the Pulay mixing,[55] can be used for updating $V_{hxc,K}$. Our method is very similar to the popular iterative method for solving KS-DFT, in which the KS Hamiltonian is diagonalized for a fixed KS potential and the KS potential is later updated using some mixing schemes.[52]

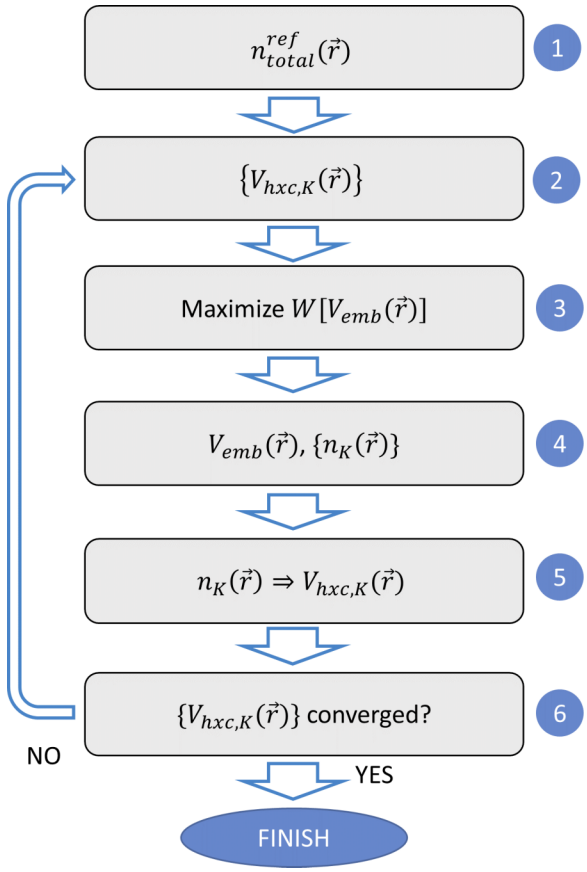

FIG. 2. The flowchart of the iterative embedding potential solver that solves for the embedding potential $V_{emb}(\vec{r})$ for a given reference density $n^{ref}_{total}(\vec{r})$. $V_{hxc,K}$ is the sum of the Hartree and XC potentials of the subsystem K. n_K is the density of the subsystem K.

For a trial $V_{hxc,K}(\vec{r})$ in the step 3, the KS Hamiltonian of the subsystem K is

$$\hat{H}_{KS,K} = -\frac{1}{2}\nabla^2 + \hat{V}_{nl,K} + \hat{V}_{emb} + \hat{V}_{ext,K} + \hat{V}_{hxc,K}, \quad (13)$$

where $V_{nl,K}$ is the nonlocal part of the pseudopotentials (if nonlocal pseudopotentials are used in calculations) and $\hat{V}_{ext,K}$ is the external potential of the subsystem K.

To work at finite temperature, the subsystem energy E_K in the W functional (Eq. (11)) is replaced by the free energy

$$F_K = \sum_j f_{K,j} \langle \phi_{K,j}, \hat{H}_{KS,K} \phi_{K,j} \rangle - TS_K, \quad (14)$$

with $\phi_{K,j}$ being the jth KS orbital of the subsystem K solved by diagonalizing $\hat{H}_{KS,K}$. $\{f_{K,j}\}$ are the occupation numbers. T is the smearing temperature used in the Fermi-Dirac smearing scheme. S_K is the electronic entropy due to the smearing and is expressed as

$$S_K = -k_B \sum_j \int (f_{K,j} \ln f_{K,j} - (1 - f_{K,j}) \ln(1 - f_{K,j})). \quad (15)$$

The accuracy of the gradient (Eq. (12)) now just depends on the accuracy of the diagonalization of the $\hat{H}_{KS,K}$. Thus accurate

gradient $g(\vec{r})$ can be obtained by tightening the threshold in the diagonalization.

C. Specifying the electron numbers in subsystems

We have three schemes to specify the electron numbers in subsystems: (a) the spin-up and spin-down electron numbers are fixed in subsystems, (b) the magnetic moment in each subsystem is relaxed, and (c) the spin-up and spin-down chemical potentials across all subsystems are equilibrated, allowing charge transfer between subsystems. In all schemes, the magnetic moment of the total system is determined by $n^{ref}_{total,\sigma}$. For the cases (a) and (b), the Fermi-Dirac smearing is used to populate electrons over the KS orbitals in subsystems.

In the case (c), the W functional is modified to be

$$W = F_S - \sum_{\sigma=\alpha,\beta} \int dr^3 n^{ref}_{total,\sigma}(\vec{r}) V_{emb,\sigma}(\vec{r}), \tag{16}$$

with

$$F_S = \sum_j f_{K,j} \langle \phi_{K,j}, \hat{H}_{KS,K} \phi_{K,j} \rangle - T S_{tot}. \tag{17}$$

F_S is the extension of the sum of the energies of all the embedded subsystems (the E_S defined in Ref. 43) to a finite temperature. The occupation numbers $\{f_{K,j}\}$ are therefore determined by distributing *all* electrons to *all* subsystems' KS orbitals according to the Fermi-Dirac statistics. The entropy is calculated as

$$S_{tot} = -k_B \sum_K \sum_j \int (f_{K,j} \ln f_{K,j} - (1 - f_{K,j}) \ln(1 - f_{K,j})),$$

with j loops over all the KS orbitals in the subsystem K. K loops over all subsystems. The expression of S_{tot} manifests that F_S is the free energy of a composite system which is the sum of all subsystems.

In order to show that there is only one minimum for the W functional in all the three cases, we now show that the W functional is concave with respect to its variable $V_{emb,\sigma}$. For the cases (a) and (b), the ground state of a subsystem is solved by minimizing its free energy (Eq. (14)) for a given V_{emb}, therefore we have $F_K[\alpha V_{emb,1} + (1-\alpha) V_{emb,2}] > \alpha F_K[V_{emb,1}] + (1-\alpha) F_K[V_{emb,2}]$ for $0 < \alpha < 1$. The linear term $\sum_\sigma \int dr^3 V_{emb,\sigma} n^{ref}_{total,\sigma}$ in W is also concave, therefore W is concave with respect to V_{emb}.

For the case (c), subsystem densities are obtained by minimizing the free energy F_S with the constraints $\sum_K N_{K,\alpha} = N_{total,\alpha}$ and $\sum_K N_{K,\beta} = N_{total,\beta}$, where $N_{total,\sigma}$ is the total electron number for spin σ. The spin-up and spin-down chemical potentials μ_α and μ_β are then the Lagrangian multipliers for these two constraints. With the similar procedure, F_S can be shown to be concave with respect to $V_{emb,\sigma}$, therefore W is concave with respect to $V_{emb,\sigma}$.

In all the three cases, the gradient for maximizing the W can be efficiently evaluated according to Eq. (12) which can be derived with the chain rule

$$\begin{aligned} g_\sigma(\vec{r}) &= \frac{\delta W}{\delta V_{emb,\sigma}(\vec{r})} \\ &= \sum_K \int dr'^3 \sum_{\sigma'} \frac{\delta F_K}{\delta n_{K,\sigma'}(\vec{r}')} \frac{\delta n_{K,\sigma'}(\vec{r}')}{\delta V_{emb,\sigma}(\vec{r})} \\ &\quad + \sum_K (n_{K,\sigma}(\vec{r}) - n^{ref}_{total,\sigma}(\vec{r})), \end{aligned} \tag{18}$$

where K loops over all subsystems.

In the case (a), we plug in the chemical potential $\mu_{K,\sigma} = \delta F_K / \delta n_{K,\sigma}$ into Eq. (18). Since the number of spin-up or spin-down electrons is fixed in each subsystem, the integral for each spin σ on the right-hand side (RHS) of Eq. (18) is then zero. In the case (b), the spin-up and spin-down chemical potentials in each subsystem are equal, since the magnetic moment in each subsystem is relaxed. The integral on the RHS of Eq. (18) is again zero, since the electron number in a subsystem is fixed. In the case (c), we plug in $\mu_\sigma = \delta F_K / \delta n_{K,\sigma}$ to the above equation, and the first term on the RHS of Eq. (18) is again zero, due to the conservation of $N_{total,\alpha}$ and $N_{total,\beta}$. Since W is concave, it then has only one maximum which is reached when the gradient is zero ($n_{total,\sigma} = \sum_K n_{K,\sigma}$).

IV. COMPUTATIONAL DETAILS

The reference densities n^{ref}_{total} are calculated with KS-DFT-GGA. Subsystem KS-DFT-GGA calculations are performed using a modified ABINIT program,[56] which takes an embedding potential as an additional external potential and diagonalizes the KS Hamiltonian using the conjugate gradient method.[52] Norm-conserving pseudopotentials were built by the fhi98pp program[57] with the default settings for the core radii. The Perdew-Burke-Ernzerhof (PBE) XC functional is employed.[58] The Fermi-Dirac smearing is used with a smearing temperature of 0.1 eV. The kinetic energy cutoffs of 600 eV, 800 eV, and 600 eV are used for the $CoCl_4^{2-}$, Fe_5, and H_2 examples, respectively. For the NiO dimer and the Fe body-centered cubic (bcc) (110) surface, a kinetic energy cutoff of 800 eV is used. The kinetic energy cutoffs used here are smaller than what they are expected to be. Since the purpose is to demonstrate the efficiency and robustness of our new iterative embedding potential solver, these relatively low kinetic energy cutoffs should not introduce any fundamental issue. All structures are relaxed using KS-DFT-PBE.

A FORTRAN90 program (named "dfet-driver") is written to conduct the flowchart in Fig. 2. The dfet-driver program calls ABINIT to perform *non-self-consistent* KS-DFT calculations to maximize the W functional. In the step 6 (Fig. 2), a vector is formed by concatenating subsystem KS potentials, as $V_{KS,all} = [V_{KS,1}, V_{KS,2}, \ldots, V_{KS,m}]$, with m being the number of subsystems. We found that the Anderson mixing[54] of $V_{KS,all}$ with a mixing parameter of 0.2 yields good convergence rates. To obtain the initial guesses of subsystem KS potentials, we perform 20 iterations of non-spin-polarized KS-DFT-PBE calculations on isolated subsystems. In the step 3 (Fig. 2), we terminate the optimization of the W functional when one of the two criteria is met: (a) the norm (g_{norm}) of the gradient $g(\vec{r})$ is reduced by five times or (b) the change

of the W is less than 1×10^{-5} hartree. To suppress the ripples in the inverted embedding potentials, embedding potentials are regularized,[59] with a penalty coefficient of 1×10^{-5} for all examples. Plots are generated using the VESTA program.[60]

We allow charge transfer between subsystems in some examples. Charged systems cannot be described exactly by the periodic boundary condition, due to the long-range Coulomb interaction between periodic images.[61] Charged subsystems are not problems in our method, since the subsystem KS potentials are fixed during the maximization of the W functional. The gradient, calculated according to Eq. (12), is always consistent with the W functional, even if the periodic boundary condition is employed.

V. RESULTS AND DISCUSSIONS

We show the performance of our iterative embedding potential solver with several spin-polarized examples. For each example, spin-polarized embedding potentials are calculated to study the stability, efficiency, and accuracy of the method.

A. Covalent system: H_2 molecule

The spin symmetry can be broken by introducing spin-polarized embedding potentials. We demonstrate this with the H_2 molecule, with each hydrogen atom being considered as a subsystem. We assign one spin-up electron in one subsystem and one spin-down electron in another subsystem. The spin-up and spin-down embedding potentials are plotted in Figs. 3(b) and 3(d). In Fig. 3(b), the spin-up embedding potential is positive on the right hydrogen to push the spin-up electron density to the left hydrogen atom and is negative on the left hydrogen atom to attract the spin-up electron density. The spin-up embedding potential produces the spin-up electron density that is *exactly* one half of the total electron density of H_2. Due to the symmetry, similar results are obtained for the spin-down embedding potential (Fig. 3(d)).

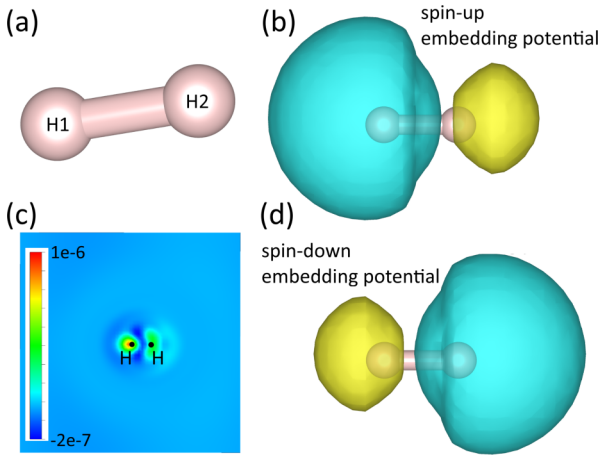

FIG. 3. (a) The structure of the H_2 molecule. Subplots (b) and (d) are the spin-up and spin-down embedding potentials. The isosurface value is 0.1 a.u. The blue represents a negative potential (−0.1 a.u.) and the yellow represents a positive embedding potential (0.1 a.u.). (c) The contour plot of the spin-up $n_{diff}(\vec{r})$. Due to the symmetry, the spin-down n_{diff} is not shown.

The convergence of our iterative embedding potential solver on this H_2 molecule is fast, and the W functional changes less than 10^{-4} hartree after 15 iterations. The quality of the embedding potential is good and can be assessed based on the difference between the reference density and the sum of subsystem electron densities, i.e.,

$$n_{diff,\sigma}(\vec{r}) = n^{ref}_{total,\sigma}(\vec{r}) - \sum_K n_{K,\sigma}(\vec{r}).$$

The contour plot of spin-up $n_{diff}(\vec{r})$ is shown in Fig. 3(c) with the plane passing through the two hydrogen atoms. The maximum density difference is on the order of 10^{-6} 1/bohr^3, indicating a good quality of the calculated embedding potential.

B. A metallic system: The Fe_5 cluster

We choose a Fe_5 cluster (Fig. 4), which has a high magnetic moment. This Fe_5 cluster is extracted from a Fe bcc (110) surface and has two layers. The top layer has one Fe atom, and the second layer has four Fe atoms. The magnetic moment on each Fe atom is similar, with an average magnetic moment $\bar{\mu}_{Fe}$ of 3.98 μ_B.

We consider two partitioning schemes which are described in Fig. 4. In both schemes, each subsystem is set to neutral in our calculations. The magnetic moment of each subsystem is manually set to $N_{natom} \times \bar{\mu}_{Fe}$, where N_{natom} is the number of Fe atoms in each subsystem.

The spin-polarized embedding potentials for the partitioning scheme I are shown in Figs. 5(a) and 5(b). The embedding potentials are negative between the two subsystems to attract electrons to form the metallic bonds. The spin-polarized electron densities are shown in Figs. 5(c)-5(f). The top Fe atom has nearly 6 spin-up and 4 spin-down electrons; therefore its spin-up electron density is almost spherical, due to the fact that its spin-up d orbitals are almost filled. We observe that the spin-down electron density of the top Fe atom is of the $d_{x^2-y^2}$ type (Fig. 5(d)). For the subsystem 2 (the lower four-Fe plane), the spin-up electron density again has no special feature, since all the spin-up d orbitals are nearly filled completely (Fig. 5(e)). Adjacent Fe atoms form the metallic bonds (Fig. 5(f)).

To better assess the convergence rate of our method, we define

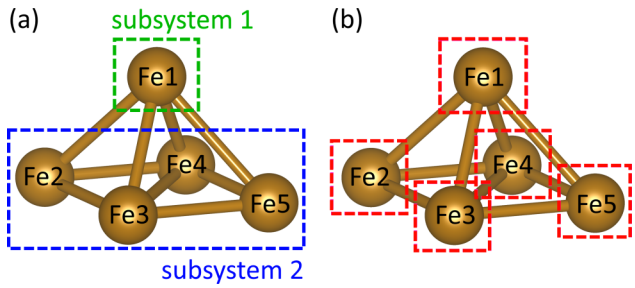

FIG. 4. The two partitioning schemes used for the Fe_5 cluster. (a) The scheme I: the top Fe atom (in the green dashed box) is the subsystem 1 and the other four Fe atoms are (in the blue dashed box) the subsystem 2. (b) The scheme II: each Fe atom is considered as a subsystem.

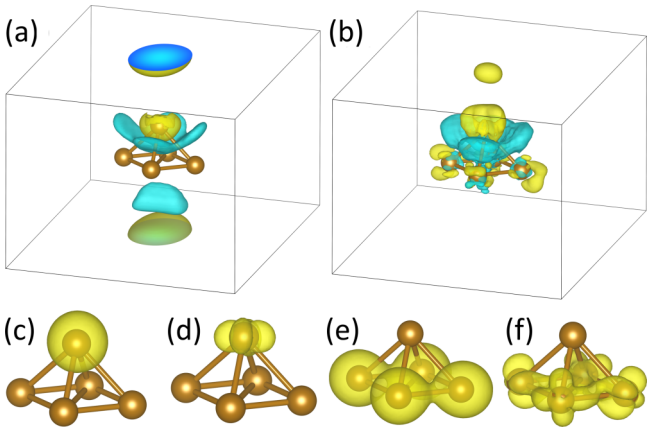

FIG. 5. (a) The spin-up and (b) spin-down embedding potentials for the Fe_5 cluster obtained for the partitioning scheme I. The isosurface value is 0.05 a.u. The blue region represents a negative (attractive) potential. The yellow region represents a positive (repulsive) potential. (c) The spin-up and (d) spin-down electron densities for the subsystem 1 (the top Fe atom). (e) The spin-up and (f) spin-down electron densities for the subsystem 2 (the lower four-Fe plane).

$$n_{conv} = \max\{|n_j^m(\vec{r}) - n_j^{m-1}(\vec{r})|\},$$

where j is the subsystem index and m is the iteration number. The change of n_{conv} with the iteration number is plotted in Figs. 6(a) and 6(b) for both partitioning schemes. The convergence rates are good. For both partitioning schemes, after about 10 iterations, n_{conv} changes less than 0.001 bohr^{-3} in all subsystems. KS-DFT can be difficult to converge for a single Fe atom, which makes it numerically challenging to solve for embedding potentials with our previous OEP method.[20] Here we observe that our iterative embedding potential solver is robust for this Fe_5 cluster which has a high magnetic moment.

The quality of the embedding potentials can depend on two factors: (1) how much penalty coefficient is employed in the OEP method for regularizing the embedding potential and (2) how stable the embedding potential solver is. In Figs. 7(a) and 7(b), the spin-up $n_{diff}(\vec{r})$ is on the order of 10^{-5} bohr^{-3} and the spin-down n_{diff} is on the order of 10^{-4} bohr^{-3}. In both cases, we observe that n_{diff} is relatively large in the core regions, but is much smaller in the bonding regions. The largest n_{diff} among the four bond midpoints (the bonds are denoted by the blue dashed lines) is 3×10^{-6} a.u. and 1.3×10^{-5} a.u. for the spin-up (Fig. 7(a)) and the spin-down cases (Fig. 7(b)), respectively. From a chemical point of view, a small n_{diff} in the bonding region indicates that the interaction between subsystems can be accurately represented by the embedding potentials. To better assess the accuracy, we compute the relative error, defined as $n_{diff}(\vec{r})/n(\vec{r})$. The largest relative error among the four bond midpoints is 1.2×10^{-4} and 5.6×10^{-4} for the spin-up case (Fig. 7(a)) and the spin-down (Fig. 7(b)) case, respectively, indicating that the reference density is well reproduced.

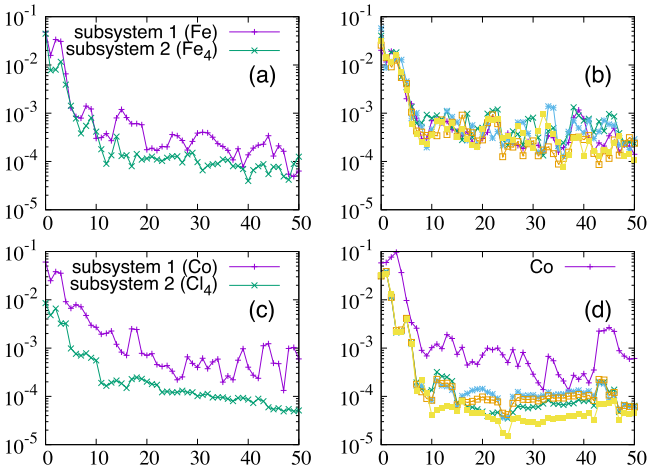

FIG. 6. The convergences of our embedding potential solver, measured by n_{conv}. The x axis is the iteration number. The subplots (a) and (b) are the results for the Fe_5 cluster. The subplot (a) is for the partitioning scheme I and the subplot (b) is for the partitioning scheme II. The subplots (c) and (d) are the results for the $CoCl_4^{2-}$ complex. The subplot (c) is for the partitioning scheme I and the subplot (d) is for the partitioning scheme II.

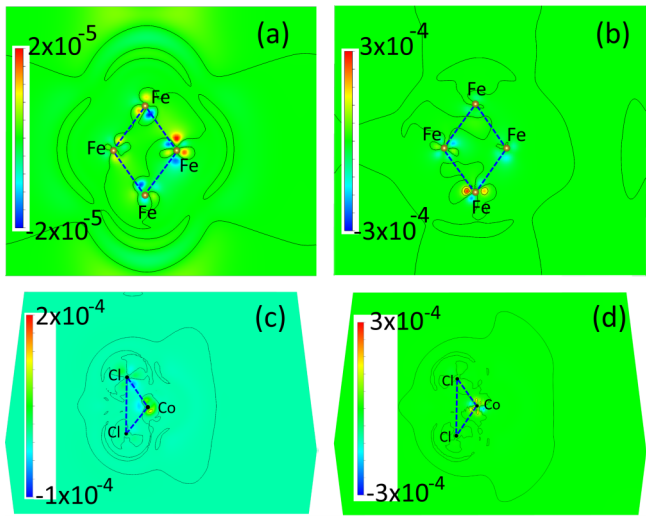

FIG. 7. The contour plots of $n_{diff}(\vec{r})$ for the Fe_5 cluster with the partitioning scheme II ((a) and (b)), and for the $CoCl_4$ complex with the partitioning scheme II ((c) and (d)). In the subplots ((a) and (b)), the slice plane is the four-Fe plane (Fig. 4). For the $CoCl_4$ case, the slice plane passes through Co and two nearby Cl atoms. The contour interval is 1×10^{-4} bohr^{-3} in all subplots. The spin-up n_{diff} are shown in (a) and (c). The spin-down n_{diff} are shown in the subplots (b) and (d).

C. An ionic system: Cobalt tetrachloride

We test our method on an ionic system: the $CoCl_4^{2-}$ complex, whose structure is shown in Fig. 8(a). Formally, each chlorine atom possesses one extra electron and is closed shell. The cobalt has a net charge of +2, and its five d orbitals are re-ordered in the way that the $d_{x^2-y^2}$ and d_{z^2} are lower in energy and are doubly occupied. The other three d orbitals are higher in energy and are singly occupied, based on the crystal field theory.[62] Approximately the Co has a magnetic moment of 3 μ_B.

To demonstrate the robustness of our method, we also consider two partitioning schemes. In both schemes, the Co is considered as one subsystem. In the partitioning scheme I, the four Cl atoms are considered as one subsystem. In the partitioning scheme II, each chlorine atom is considered as one subsystem. In both partitioning schemes, we assign five spin-up electrons and three spin-down electrons to the Co.

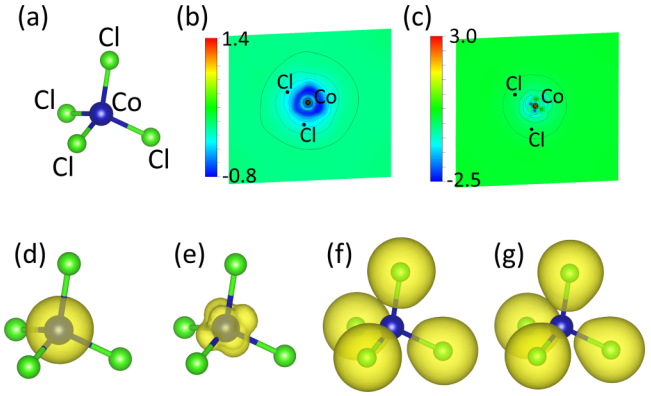

FIG. 8. (a) The structure of the $CoCl_4^{2-}$ complex. We show the results for the partitioning scheme I. (b) The contour plot of the spin-up embedding potential with the contour interval of 0.1 a.u. (c) The contour plot of the spin-down embedding potential with the contour interval of 0.3 a.u. (d) The spin-up and (e) spin-down electron densities of the subsystem 1 (the Co cation) with the isosurface value of 0.01 bohr^{-3}. (f) The spin-up and (g) spin-down electron densities of the subsystem 2 (the four Cl anions) with the isosurface value of 0.01 bohr^{-3}.

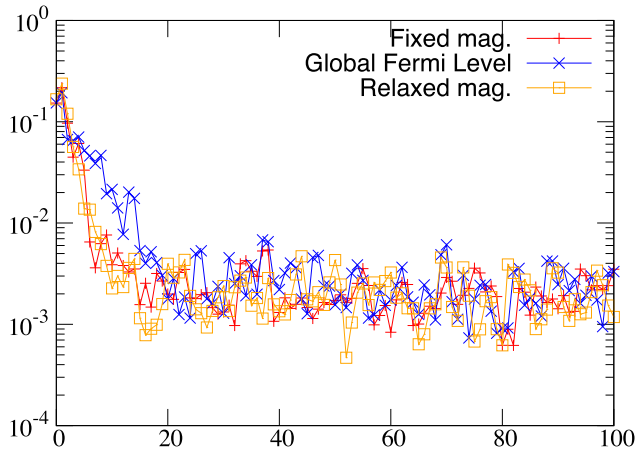

FIG. 9. The convergences of our embedding potential solver, measured by n_{conv} (in a.u.). We show the n_{conv} for the nickel subsystem. The convergences of the oxygen subsystem are similar and are not shown here. The x axis is the iteration number. We consider three cases: (a) the magnetic moment in each subsystem is fixed ("Fixed mag."), (b) the magnetic moment in each subsystem is relaxed ("Relaxed mag."), and (c) the Ni and O subsystems share common chemical potentials ("Global Fermi Level").

In the partitioning scheme I, we assign 16 spin-up and 16 spin-down electrons to the Cl_4^{4-} subsystem. In the partitioning scheme II, we assign 4 spin-up electrons and 4 spin-down electrons to each chlorine. The assignments are based on the formal charges of the Co and Cl in $CoCl_4^{2-}$.

The spin-polarized embedding potentials for the partitioning scheme I are shown in Figs. 8(b) and 8(c). The planes are spanned by the Co and the other two nearby Cl atoms. Both the spin-up and spin-down embedding potentials are approximately −0.5 hartree in the interstitial region between Co and Cl to attract Cl's electron density toward the Co. The subsystem electron densities are shown in Figs. 8(d)-8(g). The electron densities of the Cl are approximately spherical and are deformed toward the Co, due to the electrostatic attraction from the positively charged cobalt. The spin-up electron density of the Co is approximately spherical as well, since the spin-up d orbitals are almost filled. Its spin-down electron density shows more d orbital character (Fig. 8(e)).

Our method converged well on this $CoCl_4^{2-}$ complex as well. For the partitioning scheme I, after approximately 20 iterations (Fig. 6(c)), n_{conv} drops to 5×10^{-4} bohr^{-3} in the Cl_4 subsystem and to 10^{-3} in the Co subsystem. Similar convergence rate is observed for the partitioning scheme II (Fig. 6(d)). To assess the quality of the embedding potential, in Figs. 7(c) and 7(d), the spin-up and spin-down n_{diff} are both on the order of 10^{-4} bohr^{-3}. n_{diff} is large mainly near the core regions of the cobalt. At the bond midpoints (midpoints of the blue dashed lines), the spin-up and spin-down n_{diff}'s are small and are on the order of 10^{-5} a.u. and 10^{-6} a.u., respectively. Among the three bond midpoints, the largest relative error $(n_{diff}(\vec{r})/n(\vec{r}))$ is 5×10^{-4} and 4×10^{-4} for the spin-up and the spin-down cases, respectively.

D. Relax the magnetic moments of subsystems and subsystems share a common chemical potential

Our new method can also (a) relax the magnetic moment of each subsystem and (b) let all subsystems share the same chemical potential. We demonstrate these two features with a NiO molecule, whose magnetic moment is two.[63] The NiO is relaxed with KS-DFT-PBE. The relaxed bond length is 1.66 Å. We treat Ni and O as two subsystems. The convergence of our method is again fast as shown in Fig. 9. The n_{conv} in each subsystem converges to the order of 10^{-3} after 20 iterations. The mismatch between the sum of subsystem densities and the reference electron density is smaller than 4×10^{-3} bohr^{-3} after 20 steps in all cases.

The electron density of the NiO molecule is partitioned into Ni's and O's densities. After integrating their densities, we found a $0.44e$ charge transfer from Ni to O, which is close to the $0.57e$ charge transfer obtained using the Mulliken population analysis based on the correlated wave-function calculations.[63] This shows that DFET employing our new embedding potential solver could yield a physical electron density partitioning.

E. A periodic system: The Fe bcc(110) surface

Finally we consider a practical example: to calculate the embedding potential for the top layer of the Fe bcc(110) surface. The top layer is considered as the subsystem 1 and the rest of the slab is considered as the subsystem 2 (Fig. 10(a)). Subsystems are neutral and their electron numbers are fixed during the calculations. We allow the magnetic moment in each subsystem to relax. The convergence is again fast. After 11 iterations, n_{conv} drops below 10^{-4} bohr^{-3}. After four iterations, the maximum difference between the sum of subsystem electron densities and the reference total electron density drops below 2×10^{-3} bohr^{-3}. The distribution of the total magnetic moment over the two subsystems is relatively uniform. The magnetic moments are 13.3 μ_B and 36.9 μ_B in the subsystem 1 and the subsystem 2, respectively, roughly proportional to their sizes.

To better visualize the subsystems, their densities are plotted in Fig. 10. Subsystems are well separated and the

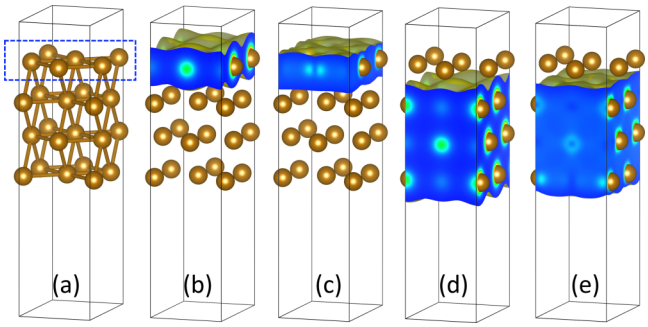

FIG. 10. (a) The Fe bcc(110) surface slab. The top layer is the subsystem 1 (in the dashed box), and the lower three layers are the subsystem 2. (b) The spin-up and (c) spin-down electron densities of the subsystem 1 (the top layer). (d) The spin-up and (e) spin-down electron densities of the subsystem 2. The isosurface values are 0.01 (in a.u.) for all subplots.

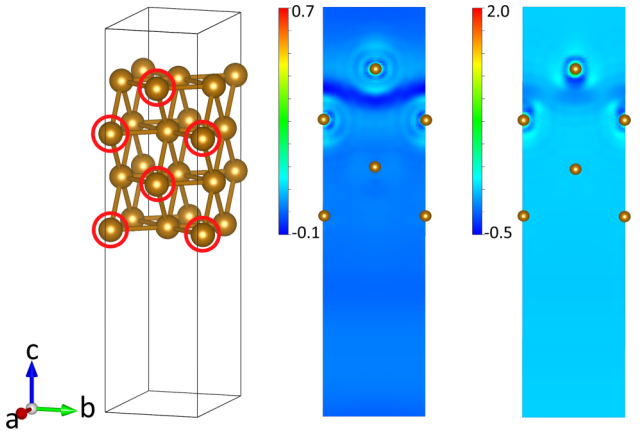

FIG. 11. The spin-up (middle) and spin-down (right) embedding potentials, with the top layer considered as the subsystem 1 and the rest Fe atoms considered as the subsystem 2. The contour plane is perpendicular to the $\vec{a}$ axis and is passing through the circled copper atoms. The circled Fe atoms on the leftmost figure are marked on the contour plots. Units are bohr^{-3}.

embedding potential is well localized at the interface (Fig. 11), which is due to the strong screening in metals.

This example is useful in practice. It is related to the modeling of these heterogeneous catalysis that involve iron, such as the Fischer-Tropsch and the Haber processes. The efficient embedding potential solver developed in this work could let us study the outer layer of a catalyst with high-level theories by replacing the subsurface with a first-principle spin-polarized embedding potential, which consequently reduces the computational cost. One possible choice is to perform embedded calculations of the top layer using the EXX+RPA. The EXX+RPA has showed good accuracy for the adsorption of molecules on transition metals;[64] however its computational scaling is poor.[65] Embedded EXX+RPA calculations could be a computationally feasible way to help us gain insight into the heterogeneous catalysis with a modest computational cost.

VI. WHY DOES THE ITERATIVE EMBEDDING POTENTIAL SOLVER WORK?

There might be two reasons for the fast convergences of the new embedding potential solver observed in above examples. The first reason is due to the use of finite temperature (the Fermi-Dirac smearing with a smearing temperature of 0.1 eV) in the non-self-consistent KS-DFT calculations on subsystems. This helps us to avoid the so-called "Fermi statistics" problem,[66] in which the frontier KS orbitals (the orbitals whose eigenvalues are close to the Fermi energy) repeatedly cross the Fermi level, which in turn makes the system's density changes radically from one iteration to the next iteration. The "Fermi statistics" problem makes the self-consistency of KS-DFT calculations difficult to reach. In practice, we observed that our embedding potential solver has trouble to converge, if the smearing temperature was set to be very small.

Another reason for the good convergences of our embedding potential solver could be that the wild changes of the subsystems densities can be effectively suppressed due to the fact that the sum of them needs to be equal to the reference density. For example, the KS-DFT took many iterations to converge for generating the reference density for the Fe_5 cluster. On the other hand, the convergence of the embedding potential solver was fast for this Fe_5 cluster.

VII. CONCLUSIONS

By extending the density functional embedding theory to finite temperature, we have largely removed the non-uniqueness of the embedding potential. A unique embedding potential makes DFET a tractable multi-physics method for material modeling. From a practical point of view, such extension is physical, since materials work at finite temperature. We then developed an efficient *iterative* method for calculating embedding potentials. Our method does not require performing self-consistent KS-DFT calculations on subsystems, and therefore avoids the convergence issue in our previous method. The performance of our method is assessed on several spin-polarized systems. Embedding potentials with good qualities were obtained. The efficient embedding potential solver developed in this work could make it possible to perform embedded CW calculations or embedded KS-DFT calculations employing advanced orbital-based XC functionals to study challenging material problems, such as the heterogeneous catalysis involving iron, cobalt, and nickel, the complex spin configurations of magnetic impurities on graphene,[67] and the proton-coupled electron-transfer catalyzed by transition metal compounds.[68]

ACKNOWLEDGMENTS

C.H. is grateful for the financial support from the Florida State University.

APPENDIX A: A PROOF FOR THE UNIQUENESS OF THE EMBEDDING POTENTIAL FOR THE CASE THAT SUBSYSTEMS ARE TREATED WITH THE GRAND CANONICAL ENSEMBLE AND FIXED ELECTRON NUMBERS

Assume that there are two embedding potentials V_{emb} and V'_{emb} that give the ground state density operators $\{\rho_A, \rho_B\}$ and

$\{\rho'_A, \rho'_B\}$, respectively. In each subsystem, chemical potential is adjusted to conserve subsystem electron numbers to be Q_A and Q_B, respectively. The adjusted chemical potentials are $\{\mu_A, \mu_B\}$ and $\{\mu'_A, \mu'_B\}$ for unprimed and primed cases. The grand canonical potential of subsystem A for the primed case is

$$\begin{aligned}\Omega'_A &= \mathrm{Tr}\rho'_A\left(H'_A - \mu'_A N + \frac{1}{\beta}\ln\rho'_A\right)\\ &< \mathrm{Tr}\rho_A\left(H'_A - \mu'_A N + \frac{1}{\beta}\ln\rho_A\right)\\ &= \Omega_A + \mathrm{Tr}\rho_A(V'_{emb} - V_{emb}) + Q_A(\mu_A - \mu'_A). \quad \text{(A1)}\end{aligned}$$

For subsystem B, we have

$$\Omega'_B < \Omega_B + \mathrm{Tr}\rho_B(V'_{emb} - V_{emb}) + Q_B(\mu_B - \mu'_B). \quad \text{(A2)}$$

Summing up above two equations, we obtain (note that chemical potentials from subsystem A and B are not equal)

$$\begin{aligned}\Omega'_A + \Omega'_B < \Omega_A + \Omega_B &\\ + \int dr^3 n_{total}(\vec{r})(V'_{emb}(\vec{r}) - V_{emb}(\vec{r}))&\\ + Q_A\Delta\mu_A + Q_B\Delta\mu_B, \quad \text{(A3)}&\end{aligned}$$

where $\Delta\mu_A = \mu_A - \mu'_A$ and $\Delta\mu_B = \mu_B - \mu'_B$. By exchanging primed and unprimed systems, we have

$$\begin{aligned}\Omega_A + \Omega_B < \Omega'_A + \Omega'_B &\\ + \int dr^3 n_{total}(\vec{r})(V_{emb}(\vec{r}) - V'_{emb}(\vec{r}))&\\ + Q_A(-\Delta\mu_A) + Q_B(-\Delta\mu_B). \quad \text{(A4)}&\end{aligned}$$

Summing up Eqs. (A3) and (A4), we reach $0 < 0$, which is false. Therefore the embedding potential is unique.

APPENDIX B: THE MINIMUM OF THE HELMHOLTZ FREE ENERGY FUNCTIONAL IS UNIQUE

Our proof is a straightforward extension of Mermin's work on grand canonical ensemble DFT. We consider $\rho \neq \rho_0$ and define a λ dependent density matrix as

$$\rho_\lambda = \exp(-\beta(H + \lambda\Delta))/\mathrm{Tr}\exp(-\beta(H + \lambda\Delta)),$$

with $\Delta = -\frac{1}{\beta}\ln\rho - H$. It is easy to check that ρ_λ connects ρ and ρ_0 as λ varies from 0 to 1. Similarly, we define a λ-dependent Helmholtz energy to connect $A[\rho]$ and $A[\rho_0]$ as λ varies from 0 to 1 as

$$A[\rho_\lambda] = \mathrm{Tr}\rho_\lambda(H + \lambda\Delta + \frac{1}{\beta}\ln\rho_\lambda) - \lambda\mathrm{Tr}\rho_\lambda\Delta. \quad \text{(B1)}$$

We will show that $A[\rho] > A[\rho_0]$. The difference between $A[\rho]$ and $A[\rho_0]$ can be formally written as

$$A[\rho] - A[\rho_0] = \int_0^1 \frac{d}{d\lambda}A[\rho_\lambda]d\lambda. \quad \text{(B2)}$$

The first term on the RHS of Eq. (B1) is the Helmholtz free energy of the Hamiltonian $H + \lambda\Delta$, with ρ_λ being the stationary point. Therefore, to calculate Eq. (B2), only the *partial* derivative with respect to λ is needed for the first term on the RHS of Eq. (B1). Eq. (B2) then becomes $\frac{d}{d\lambda}A[\rho_\lambda] = -\lambda\mathrm{Tr}\left(\frac{d}{d\lambda}\rho_\lambda\right)\Delta$. By setting the chemical potential $\mu = 0$, the steps A7-A12 in Ref. 45 can be followed to show

$$\frac{d}{d\lambda}A[\rho_\lambda] = \lambda\int_0^\beta d\beta'\langle y^\dagger y\rangle_\lambda, \quad \text{(B3)}$$

where $y(\lambda) = \Delta_\lambda(\frac{1}{2}\beta') - \langle\Delta\rangle_\lambda$. Eq. (B3) is always non-negative and is only zero when $y = 0$. For $y = 0$, Δ must be an identity matrix multiplied by a constant, which gives $\rho_0 = \rho$. Therefore, for $\rho_0 \neq \rho$, Eq. (B3) is always positive. We therefore have showed that for canonical ensemble, ρ_0, the stationary point of the $A[\rho]$ is the *only* global minimum of $A[\rho]$.

[1] W. Kohn, Phys. Rev. Lett. **76**, 3168 (1996).
[2] E. Prodan and W. Kohn, Proc. Natl. Acad. Sci. U. S. A. **102**, 11635 (2005).
[3] P. Hohenberg and W. Kohn, Phys. Rev. **136**, B864 (1964).
[4] W. Kohn and L. J. Sham, Phys. Rev. **140**, A1133 (1965).
[5] W. Yang, Phys. Rev. Lett. **66**, 1438 (1991).
[6] D. R. Bowler and T. Miyazaki, Rep. Prog. Phys. **75**, 036503 (2012).
[7] B. G. Dick and A. W. Overhauser, Phys. Rev. **112**, 90 (1958).
[8] P. V. Sushko, A. L. Shluger, and C. A. Catlow, Surf. Sci. **450**, 153 (2000).
[9] A. Redondo, W. A. Goddard, C. A. Swarts, and T. C. McGill, J. Vac. Sci. Technol. **19**, 498 (1981).
[10] Y. Zhang, T.-S. Lee, and W. Yang, J. Chem. Phys. **110**, 46 (1999).
[11] J. E. Inglesfield, J. Phys. C: Solid State Phys. **14**, 3795 (1981).
[12] J. E. Inglesfield, J. Phys.: Condens. Matter **20**, 095215 (2008).
[13] F. R. Manby, M. Stella, J. D. Goodpaster, and T. F. Miller, J. Chem. Theory Comput. **8**, 2564 (2012).
[14] G. Knizia and G. K.-L. Chan, Phys. Rev. Lett. **109**, 186404 (2012).
[15] N. Govind, Y. Wang, A. da Silva, and E. Carter, Chem. Phys. Lett. **295**, 129 (1998).
[16] N. Govind, Y. A. Wang, and E. A. Carter, J. Chem. Phys. **110**, 7677 (1999).
[17] T. Klüner, N. Govind, Y. A. Wang, and E. A. Carter, Phys. Rev. Lett. **86**, 5954 (2001).
[18] P. Huang and E. A. Carter, Annu. Rev. Phys. Chem. **59**, 261 (2008).
[19] F. Libisch, C. Huang, and E. A. Carter, Acc. Chem. Res. **47**, 2768 (2014).
[20] C. Huang, M. Pavone, and E. A. Carter, J. Chem. Phys. **134**, 154110 (2011).
[21] F. Libisch, C. Huang, P. Liao, M. Pavone, and E. A. Carter, Phys. Rev. Lett. **109**, 198303 (2012).
[22] S. Mukherjee, F. Libisch, N. Large, O. Neumann, L. V. Brown, J. Cheng, J. B. Lassiter, E. A. Carter, P. Nordlander, and N. J. Halas, Nano Lett. **13**, 240 (2013).
[23] G. Senatore and K. R. Subbaswamy, Phys. Rev. B **34**, 5754 (1986).
[24] M. D. Johnson, K. R. Subbaswamy, and G. Senatore, Phys. Rev. B **36**, 9202 (1987).
[25] P. Cortona, Phys. Rev. B **44**, 8454 (1991).
[26] T. A. Wesolowski and A. Warshel, J. Phys. Chem. **97**, 8050 (1993).
[27] T. A. Wesolowski and J. Weber, Chem. Phys. Lett. **248**, 71 (1996).
[28] J. Nafziger and A. Wasserman, J. Phys. Chem. A **118**(36), 7623 (2014).
[29] A. Severo Pereira Gomes and C. R. Jacob, Annu. Rep. Prog. Chem., Sect. C: Phys. Chem. **108**, 222 (2012).
[30] C. R. Jacob and J. Neugebauer, Wiley Interdiscip. Rev.: Comput. Mol. Sci. **4**, 325 (2014).
[31] A. Krishtal, D. Sinha, A. Genova, and M. Pavanello, J. Phys.: Condens. Matter **27**, 183202 (2015).
[32] T. A. Wesolowski, S. Shedge, and X. Zhou, Chem. Rev. **115**, 5891 (2015).
[33] T. A. Wesolowski, H. Chermette, and J. Weber, J. Chem. Phys. **105**, 9182 (1996).
[34] T. A. Wesolowski, J. Chem. Phys. **106**, 8516 (1997).
[35] S. Sharifzadeh, P. Huang, and E. A. Carter, Chem. Phys. Lett. **470**, 347 (2009).
[36] J. Neugebauer, C. R. Jacob, T. A. Wesolowski, and E. J. Baerends, J. Phys. Chem. A **109**, 7805 (2005).
[37] C. R. Jacob, J. Neugebauer, L. Jensen, and L. Visscher, Phys. Chem. Chem. Phys. **8**, 2349 (2006).
[38] R. E. Bulo, C. R. Jacob, and L. Visscher, J. Phys. Chem. A **112**, 2640 (2008).
[39] O. Roncero, M. P. de Lara-Castells, P. Villarreal, F. Flores, J. Ortega, M. Paniagua, and A. Aguado, J. Chem. Phys. **129**, 184104 (2008).

[40]P. Elliott, K. Burke, M. H. Cohen, and A. Wasserman, Phys. Rev. A **82**, 024501 (2010).
[41]S. Fux, C. R. Jacob, J. Neugebauer, L. Visscher, and M. Reiher, J. Chem. Phys. **132**, 164101 (2010).
[42]J. D. Goodpaster, N. Ananth, F. R. Manby, and T. F. Miller, J. Chem. Phys. **133**, 084103 (2010).
[43]M. H. Cohen and A. Wasserman, J. Stat. Phys. **125**, 1121 (2006).
[44]W. Yang, P. W. Ayers, and Q. Wu, Phys. Rev. Lett. **92**, 146404 (2004).
[45]N. D. Mermin, Phys. Rev. **137**, A1441 (1965).
[46]H. Eschrig, Phys. Rev. B **82**, 205120 (2010).
[47]J. P. Perdew and K. Schmidt, AIP Conf. Proc. **577**, 1 (2001).
[48]J. P. Perdew and A. Zunger, Phys. Rev. B **23**, 5048 (1981).
[49]J. P. Perdew, R. G. Parr, M. Levy, and J. L. Balduz, Phys. Rev. Lett. **49**, 1691 (1982).
[50]A. J. Cohen, P. Mori-Snchez, and W. Yang, Chem. Rev. **112**, 289 (2012).
[51]R. Parr and W. Yang, *Density-Functional Theory of Atoms and Molecules* (Oxford University Press, USA, 1989).
[52]M. C. Payne, M. P. Teter, D. C. Allan, T. A. Arias, and J. D. Joannopoulos, Rev. Mod. Phys. **64**, 1045 (1992).
[53]S. Kümmel and L. Kronik, Rev. Mod. Phys. **80**, 3 (2008).
[54]D. G. Anderson, J. Assoc. Comput. Mach. **12**, 547 (1965).
[55]P. Pulay, Chem. Phys. Lett. **73**, 393 (1980).
[56]X. Gonze, B. Amadon, P.-M. Anglade, J.-M. Beuken, F. Bottin, P. Boulanger, F. Bruneval, D. Caliste, R. Caracas, M. Côté, T. Deutsch, L. Genovese, P. Ghosez, M. Giantomassi, S. Goedecker, D. Hamann, P. Hermet, F. Jollet, G. Jomard, S. Leroux, M. Mancini, S. Mazevet, M. Oliveira, G. Onida, Y. Pouillon, T. Rangel, G.-M. Rignanese, D. Sangalli, R. Shaltaf, M. Torrent, M. Verstraete, G. Zerah, and J. Zwanziger, Comput. Phys. Commun. **180**, 2582 (2009).
[57]M. Fuchs and M. Scheffler, Comput. Phys. Commun. **119**, 67 (1999).
[58]J. P. Perdew, K. Burke, and M. Ernzerhof, Phys. Rev. Lett. **77**, 3865 (1996).
[59]T. Heaton-Burgess, F. A. Bulat, and W. Yang, Phys. Rev. Lett. **98**, 256401 (2007).
[60]K. Momma and F. Izumi, J. Appl. Crystallogr. **44**, 1272 (2011).
[61]G. Makov and M. C. Payne, Phys. Rev. B **51**, 4014 (1995).
[62]J. H. Van Vleck, Phys. Rev. **41**, 208 (1932).
[63]S. P. Walch and W. A. Goddard, J. Am. Chem. Soc. **100**, 1338 (1978).
[64]L. Schimka, J. Harl, A. Stroppa, A. Grüneis, M. Marsman, F. Mittendorfer, and G. Kresse, Nat. Mater. **9**, 741 (2010).
[65]M. Kaltak, J. Klimeš, and G. Kresse, Phys. Rev. B **90**, 054115 (2014).
[66]J. Harris, Phys. Rev. A **29**, 1648 (1984).
[67]A. V. Krasheninnikov, P. O. Lehtinen, A. S. Foster, P. Pyykkö, and R. M. Nieminen, Phys. Rev. Lett. **102**, 126807 (2009).
[68]J. J. Concepcion, J. W. Jurss, J. L. Templeton, and T. J. Meyer, J. Am. Chem. Soc. **130**, 16462 (2008).